1   **Multiscale cardiac imaging to capture the whole heart and its internal cellular**
2   **architecture, with applications to congenital heart disease**

3   Graham Rykiel[1], Claudia S. López[1,3], Jessica L. Riesterer[1,3], Ian Fries[1], Sanika Deosthali[1], Katherine
4   Courchaine[1], Alina Maloyan[2], Kent Thornburg[2], Sandra Rugonyi[1,2] *

5   [1.] Biomedical Engineering, [2.] Center for Developmental Health, Knight Cardiovascular Institute, [3.] Multiscale
6   Microscopy Core, Oregon Health & Science University, Portland Oregon, USA
7
8   * Corresponding author: Sandra Rugonyi, rugonyis@ohsu.edu

9   **Abstract**

10 Efficient cardiac pumping depends on the morphological structure of the heart, but also on its
11 sub-cellular (ultrastructural) architecture, which enables cardiac contraction. In cases of
12 congenital heart defects, localized sub-cellular disruptions in architecture that increase the risk
13 of heart failure are only starting to be discovered. This is in part due to a lack of technologies
14 that can image the three dimensional (3D) heart structure, assessing malformations; and its
15 ultrastructure, assessing disruptions. We present here a multiscale, correlative imaging
16 procedure that achieves high-resolution images of the whole heart, using 3D micro-computed
17 tomography (micro-CT); and its ultrastructure, using 3D scanning electron microscopy (SEM).
18 This combination of technologies has not been possible before in imaging the same cardiac
19 sample due to the heart large size, even when studying small fetal and neonatal animal models
20 ($\sim$5x5x5mm^3). Here, we achieved uniform fixation and staining of the whole heart, without losing
21 ultrastructural preservation (at the nm resolution range). Our approach enables multiscale
22 studies of cardiac architecture in models of congenital heart disease and beyond.

23

Introduction

24

25   Congenital heart disease (CHD), which manifests as a morphologically defective heart, affects
26   about 1% of newborn babies, and remains the primary cause of non-infectious children mortality
27   in the developed world [1,2]. While CHD mortality rates have been dramatically reduced in recent
28   years thanks to advances in surgical practice and interventional technologies [1,3], CHD patients
29   continue to be at an increased risk of developing heart failure at a much younger age than the
30   general population [4]. Despite early indicators of success, heart failure continues to take the lives
31   of young children with CHD: 10 to 25% of newborns with a critical heart defect do not survive
32   the first year, and 44% do not survive to 18 years of age [5,6]. This unfortunate trend points to
33   cardiac deficiencies in CHD that are not yet understood [7].

34   While the structural (morphological or "geometrical") characteristics of heart malformations have
35   been extensively studied, it is largely unknown whether cardiac cells from malformed hearts are
36   normal or to what extent they are compromised. Recent studies reveal an abnormal orientation
37   of myocardial cells (the heart muscle cells) within CHD hearts [8-10]. Myocardial cells are
38   elongated, cylindrical-like cells, that contract along their long axis. In a normal heart, myocardial
39   cells arrange in sheet-like layers with their long axes in parallel to each other forming an
40   elliptical pattern [11,12]. Newly developed contrast episcopic microscopy and synchro micro-CT
41   imaging techniques, enable non-destructive analyses of banked human fetal and neonatal
42   hearts with CHD. [9,10] These studies are revealing myocardial disarray in CHD (with respect to
43   their normal counterparts) that very likely affect cardiac function after surgical repair, and that
44   have been ignored when planning treatment strategies for CHD patients. In addition to changes
45   in the myocardial organization, the sub-cellular contraction machinery of myocardial cells (e.g
46   the myofibrils that contract the cell; and the mitochondria that provide energy for contraction)
47   may also be compromised in CHD, affecting heart function. The extent to which the cells of
48   malformed hearts exhibit deficiencies is unknown [8,10,13]. This is in part due to limitations of
49   existing technologies that have not achieved precise multiscale mapping to decipher the
50   association between structural and cellular deficiencies in the heart and beyond.

51   We describe here a novel, correlative multiscale imaging procedure that combines imaging of
52   whole heart morphology and its sub-cellular organization (ultrastructural architecture). Our
53   multiscale procedure uses micro computed tomography (micro-CT) imaging to capture heart
54   morphology at micrometer resolution, and scanning electron microscopy (SEM) to capture
55   cardiac tissue ultrastructure at nanometer resolution. Current SEM technologies allow for three-
56   dimensional (3D) imaging of sub-cellular architecture, enabling reconstruction and quantification
57   of ultrastructural features within a tissue volume [14-16]. Among 3D SEM methods, we have
58   selected serial block-face SEM (SBF-SEM) for ultrastructural imaging, as it allows 3D imaging of
59   relatively large volumes (sample size 40x60x40 μm^3). The methodology we present herein
60   improves upon previous protocols by achieving uniform staining of a relatively large heart
61   sample (3-4 mm wide, 5-6 mm long), circumventing micro-CT x-ray penetration issues, and
62   allowing sample screening and selection prior to full sample preparation. Our multiscale imaging,
63   further, enables mapping of structural and ultrastructural heart features.

64   As proof of concept, we applied our developed multiscale imaging procedure to two embryonic

65   chick hearts. These hearts were collected at stages corresponding to about 5-6 months of

66   human fetal development, when the heart is already formed but maturing in preparation for

67   birth/hatching. We imaged: 1) a control heart with no structural defects; and 2) a heart with

68   tetralogy of Fallot (TOF), a combination of structural heart malformations found in humans [17,18].

69   Our results suggest differences in the ultrastructure of these two hearts, emphasizing the need

70   for a multiscale approach to deepen our understanding of CHD and enable the development of

71   effective strategies to combat heart failure in CHD.

72   **Results**

73   <u>Overview of multiscale imaging procedure:</u>

74   To achieve multiscale imaging we followed a four-step protocol (see **Figure 1**; details in

75   Methods). Briefly, in **Step 1** the heart was excised, homogeneously fixed and stained for micro-

76   CT. Initial staining followed a modified ferrocyanide-reduced osmium–thiocarbohydrazide–

77   osmium (ROTO) protocol [19-21] typically used for electron microscopy (EM) sample preparation.

78   Three-dimensional micro-CT images (10 μm resolution) confirmed uniform ROTO staining of the

79   whole heart and provided morphological cardiac details. At this time the heart samples were

80   stored until further processing, enabling selection of specific samples for full processing based

81   on micro-CT scans. **Step 2** finalized the preparation of the whole heart for SBF-SEM by post-

82   staining the hearts with uranyl acetate and lead aspartate and then embedding them in a resin

83   block. Uniform staining was confirmed on a semithin (250 nm) section of the block, which also

84   determined ultrastructural quality and enabled registration to micro-CT images. In **Step 3**, a slab

85   of the sample was cut and sectioned around a specific region of interest (ROI, ~500x500 μm^2)

86   from which sub-ROIs for 3D SBF-SEM imaging (~ 40x60 μm^2) were selected. In **Step 4**, 3D

87   SBF-SEM datasets were acquired (10 nm lateral resolution and 40 nm depth resolution).

88
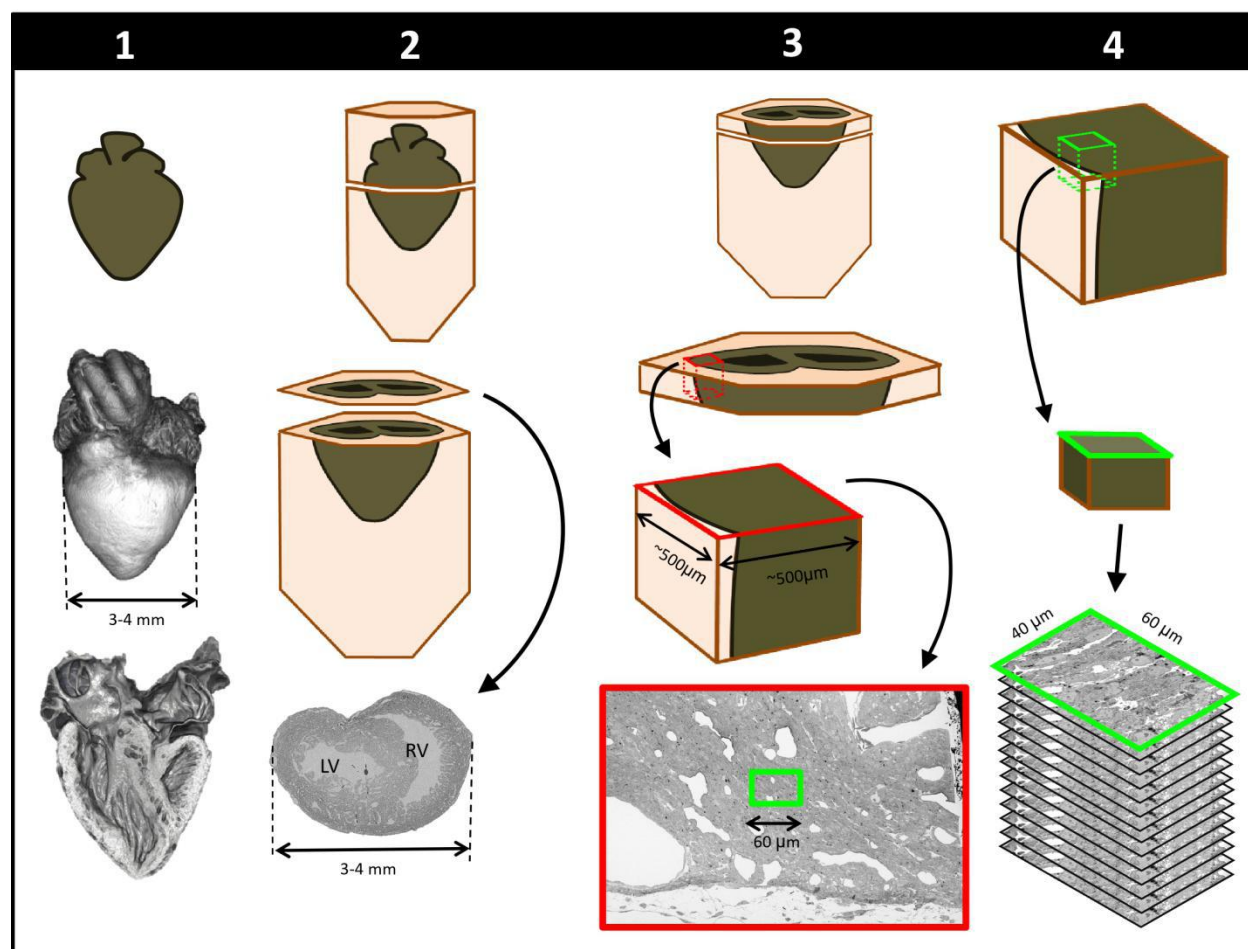
Figure 1: Schematics of steps performed to achieve cardiac multiscale imaging, which yields both 3D whole-heart images and 3D ultrastructural images from the same heart. Columns depict the four steps employed. In **Step 1**, the heart is post-fixed with osmium tetroxide to provide contrast for 3D micro-CT images of the whole heart (middle row). Digital sections of the micro-CT scans (bottom row) reveal the heart's interior and allow for cardiac phenotyping and assessment of stain penetration. In **Step 2**, contrast staining is finalized and the resin block in which the heart is embedded is sectioned to reach a plane of interest (bottom row). In **Step 3**, after cutting a slab of the sample, a region of interest (ROI) is sectioned from the slab, mounted, and then scanned by SEM backscattered imaging methods to aid in the selection of sub-ROIs (for example, the sub-ROI highlighted in green). In **Step 4**, the selected sub-ROI 3D SBF-SEM images are acquired by progressively sectioning and imaging 40nm thick layers.

Whole heart imaging:

We obtained 3D micro-CT images of the whole heart, featuring both external and internal structures at 10 μm resolution (**Figure 2**; **Step 1** in **Figure 1**). Despite the relatively large dimensions of the heart (5-6 mm long; 3-4 mm wide), tissue contrast was uniform across the heart walls and septae and allowed us to visualize the microstructural details of the heart chambers, valves, and great arteries.

108

109
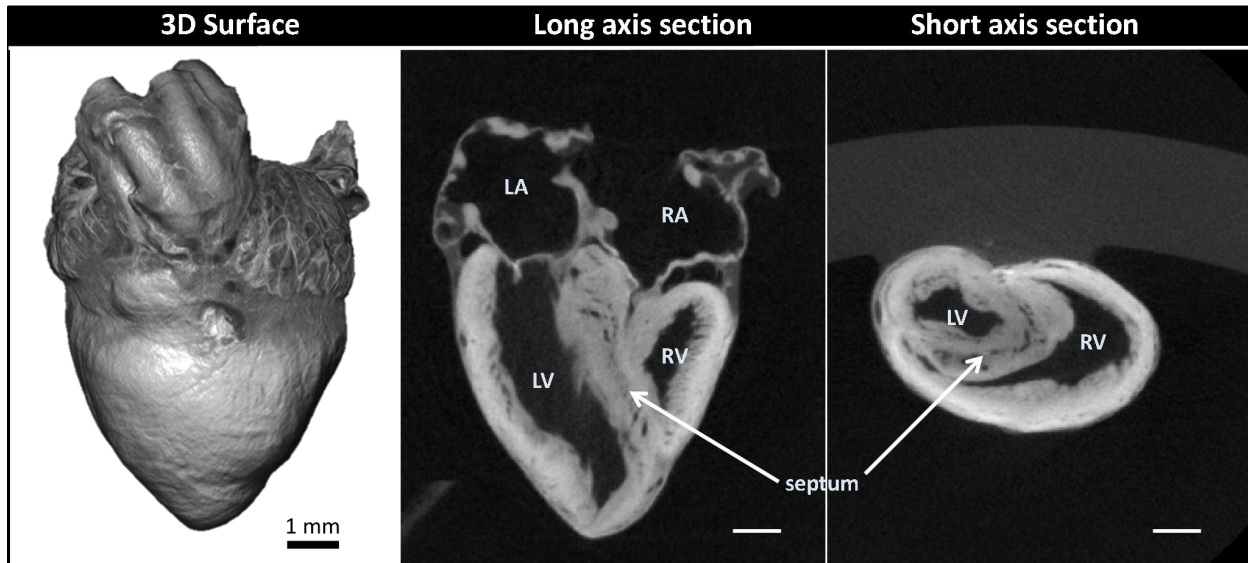
Figure 2: Micro-computed tomography (micro-CT) images of a chicken embryo normal heart. The contrast was achieved by following **Step 1** of our correlative multiscale imaging protocol (**Figure 1**). **From left to right:** External 3D surface of the heart; cardiac section along the heart's long axis (coronal section); cardiac section across the heart's short axis (transverse section). Cardiac sections show uniform staining across cardiac walls, and reveal the heart internal and external microstructure. LA: left atrium; LV: left ventricle; RA: right atrium; RV: right ventricle. Scale bars 1mm.
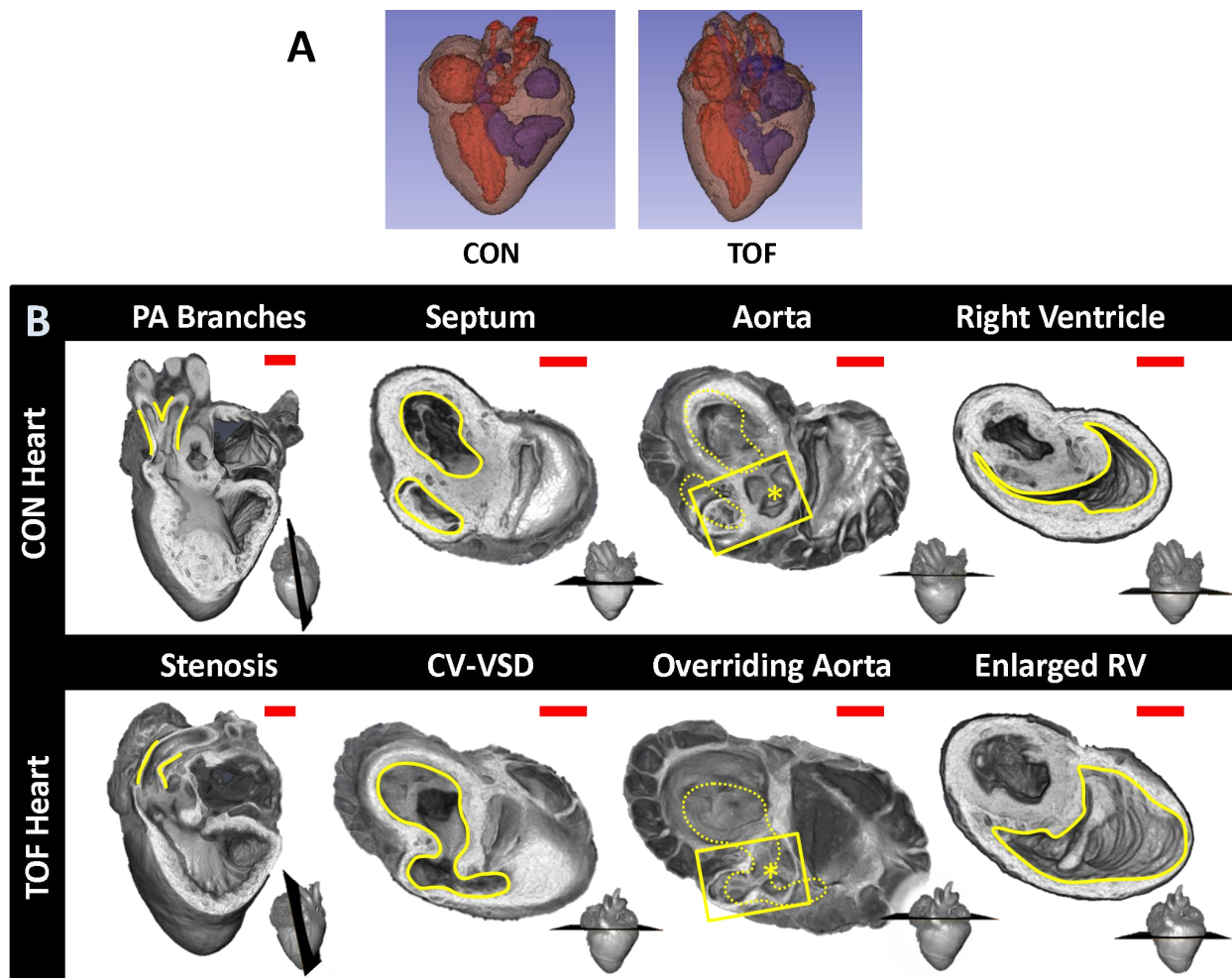
118

Cardiac structure analysis from 3D micro-CT images:

Micro-CT images were used to explore the structural characteristics of several chick hearts, to select two hearts for subsequent SBF-SEM imaging and analysis. We selected: 1) a normal heart; and 2) a heart exhibiting TOF malformation. In a normal heart, blood in the left ventricle (LV) and right ventricle (RV) is separated by an interventricular septum; the pulmonary valve and pulmonary artery connect to the RV, which pumps blood to the lungs; and the aortic valve and aorta connect to the LV, which pumps blood to the body. TOF is characterized by a combination of 4 defects: i) ventricular septal defect, which is a hole in the interventricular septum; ii) overriding aorta, a change in the position of the aorta such that it sits in the middle of the two ventricles, on top of the ventricular septal defect; iii) pulmonary stenosis or atresia, a narrowing or closure of the pulmonary artery or pulmonary valve; and iv) RV hypertrophy, a thickening and enlargement of the RV wall. RV hypertrophy in TOF, however, develops over time as the stenosis of the pulmonary artery increases pressure in the RV after birth [17] and was not present in the heart examined in this study (see **Figure 3** for a comparison of the selected normal and TOF hearts). The TOF heart analyzed here featured supravalvular pulmonary stenosis, a ventricular septal defect, and an overriding aorta. The right ventricle was enlarged and thin-walled compared to the control heart (**Figure 3**). Further, the TOF heart was missing the right branch of the pulmonary artery. In humans, this rare condition, called unilateral

Page | 5

137   absence of a pulmonary artery, is known to occur in conjunction with TOF or cardiac septal
138   defects [22].

139

A

CON   TOF

B

| PA Branches | Septum | Aorta | Right Ventricle |

CON Heart

| Stenosis | CV-VSD | Overriding Aorta | Enlarged RV |

TOF Heart

140

141   **Figure 3:** Comparison of micro-CT images of the two hearts selected for this study. **(A)**
142   Segmentations showing the heart morphology for the normal, control (CON) heart and the TOF
143   heart. Red: lumen of the left atrium and ventricle as well as aorta; Blue: lumen of the right atrium
144   and ventricle as well as pulmonary artery; Brown: heart tissue. **(B)** Detailed comparison of the
145   two hearts. Each column compares a cardiac feature (highlighted in yellow) between the hearts.
146   The position of the plane along which the tissue was cut for display is shown at the bottom right
147   of each image. From left to right: **Pulmonary artery (PA) branches:** On the control heart, the
148   PA is bifurcated (yellow lines) whereas the left branch of the PA is absent in the TOF heart. The
149   remaining PA of the TOF heart exhibits supravalvular stenosis (yellow lines). **Septum:** The
150   ventricles (yellow lines) in the control heart are discrete, separated by an intact interventricular
151   septum, whereas the TOF heart shows a conoventricular septal defect (CV-VSD). **Aorta:** In the
152   control heart the aortic valve (asterisk) is connected to the left ventricle, whereas in the TOF
153   heart the aortic valve is positioned directly over the VSD. Dotted yellow lines show the position
154   of yellow lines in the septum column. **Right Ventricle (RV):** The RV (yellow lines) is significantly
155   larger in the TOF heart than in the control heart, and features thinner walls. Scale bars = 1mm.

156

157   <u>Cardiac ultrastructural imaging:</u>

158   We chose to characterize the ultrastructure architecture of the selected hearts at approximately
159   the transverse section at which the heart width (from LV to RV wall) is maximal, also referred to
160   as the equatorial plane. Images of semithin cross-sections for each heart (**Figure 4**, top row;
161   corresponding to **Step 2** in **Figure 1**) show that staining was uniform, indicating successful stain
162   penetration through the heart tissues. Please note that the transverse section of the TOF heart
163   was below the ventricular septal defect and thus exhibits a continuous septum.

164   Using the semithin section SEM images, ROIs from the hearts were selected. For this study, we
165   selected two ROIs within the heart LV, denoted by ROI A and ROI B. After cutting the sample,
166   the ROIs were first imaged with SBF-SEM at low resolution (65-80 nm lateral resolution; **Step 3**
167   in **Figure 1**), from which sub-ROIs were further selected (see **Figure 4**). These sub-ROIs
168   (~40x60 μm^2) were imaged at 10 nm lateral resolution, and we acquired 800-1000 images in
169   depth (with ~40nm of depth distance, thus 32 to 40 μm in depth). These high-resolution images
170   showed the conservation of ultrastructural features (see **Figure 5**). Images exhibited continuous
171   nuclear membranes, intact mitochondria, and defined myofibrils, indicating that we achieved
172   both appropriate and uniform fixation and staining of the hearts with our protocol.

173
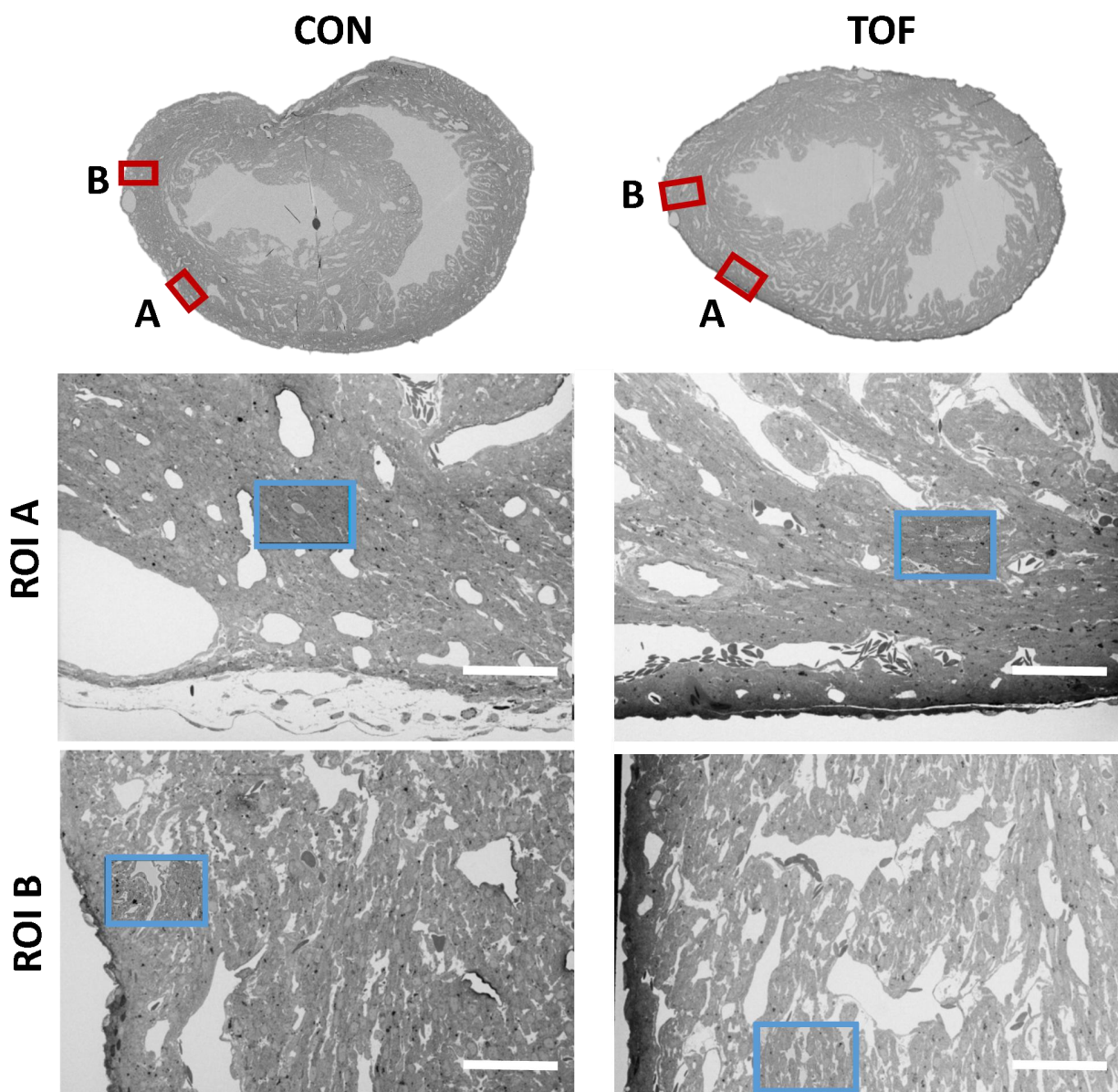
Figure 4: SBF-SEM images of the control (CON, left) and TOF (right) hearts, indicating the location of imaging. Overview scans from semithin transverse sections of each heart (**top row**) were used to confirm uniform stain penetration and the location of 2 ROIs per heart (ROI A and ROI B) further analyzed (red boxes). Semithin sections are not to scale. Blood vessels and trabeculae served as landmarks for accurate positioning of the ROIs and sub-ROIs. The sub-ROIs corresponding to ROI A (**second row**), were fully segmented (nuclei, extracellular space, myofibrils, and mitochondria). However, the sub-ROIs corresponding to ROI B (**third row**) were only partially segmented (only a fraction of the images in the stack were segmented) for quantification purposes. Scale bars 60 microns.

187
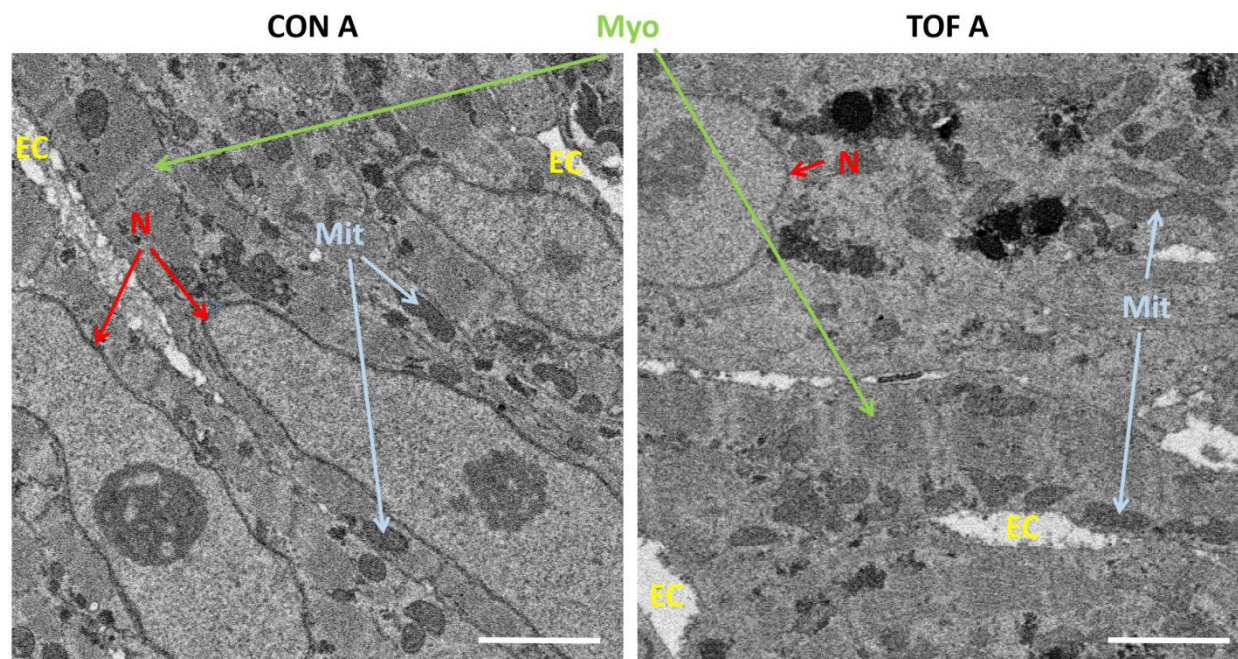
Figure 5: Detail of high-resolution SBF-SEM images obtained. The pictures depict small regions within the selected sub-ROIs from region A of the control (CON) and TOF hearts. Nuclear membranes (N) are depicted, as well as myofibrils (Myo) and mitochondria (Mit). Finally, the extracellular space (EC) is also visible. Scale bars 2 microns.

192

<u>3D SBF-SEM image reconstruction:</u>

SBF-SEM image stacks provided 3D volumetric recontructions of sub-ROIs. While volumetric image resolution was not isotropic (10 nm lateral resolution versus 40 nm depth resolution), ultrastructural features could be visualized from any angle of view within the reconstructed images (see **Figure 6**). Thus SBF-SEM images allowed us to visualize the orientation and organization of nuclei, myofibrils, and mitochondria (among other features) in heart tissue samples.

200
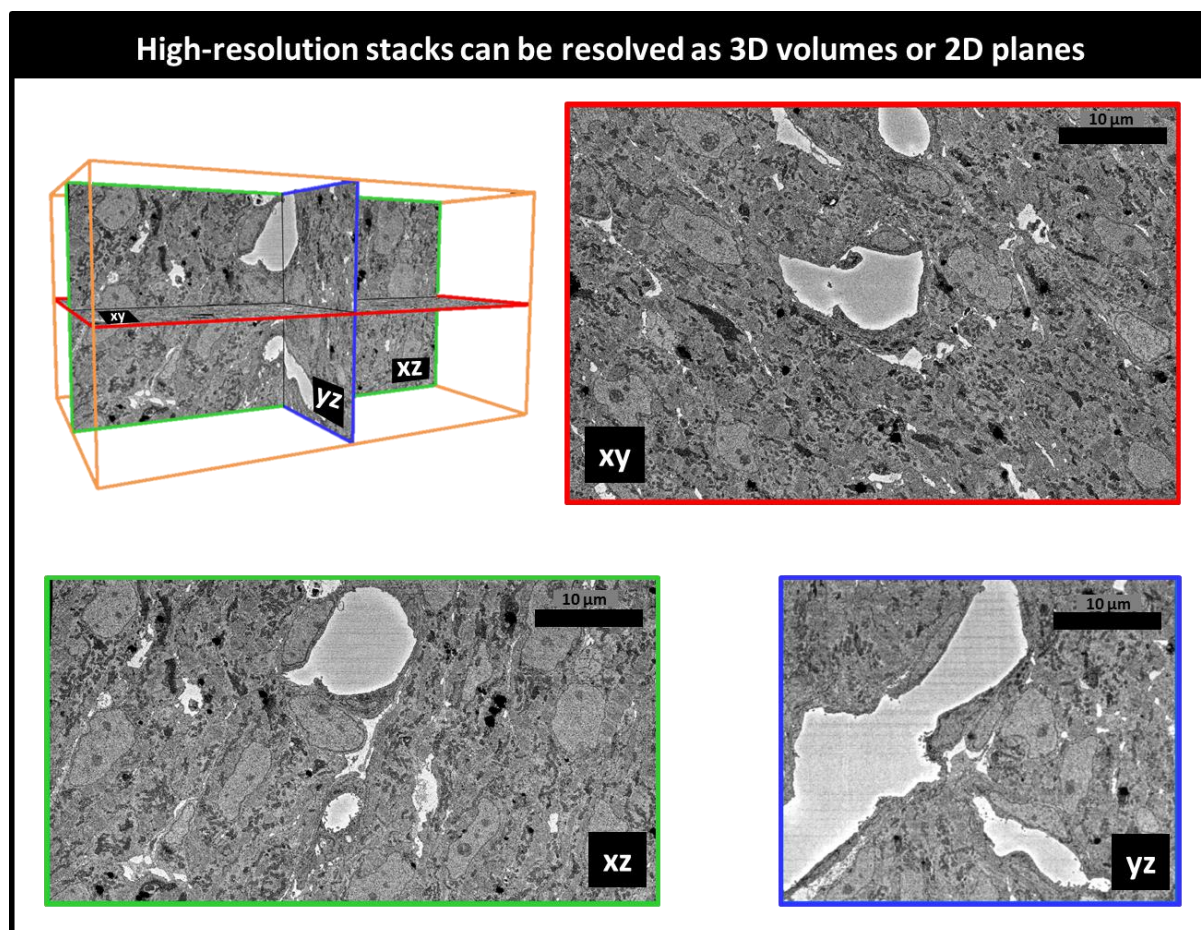
Figure 6: Example 3D reconstruction of SBF-SEM image stack acquired from the control heart. **xy** is the imaging plane, acquired at 10 nm lateral resolution. z is the depth direction, with xy images acquired every 40 nm. **xz** and **yz** are reconstructed images depicting continuity of the image stack along the z-axis (depth). Scale bars = 10 microns.
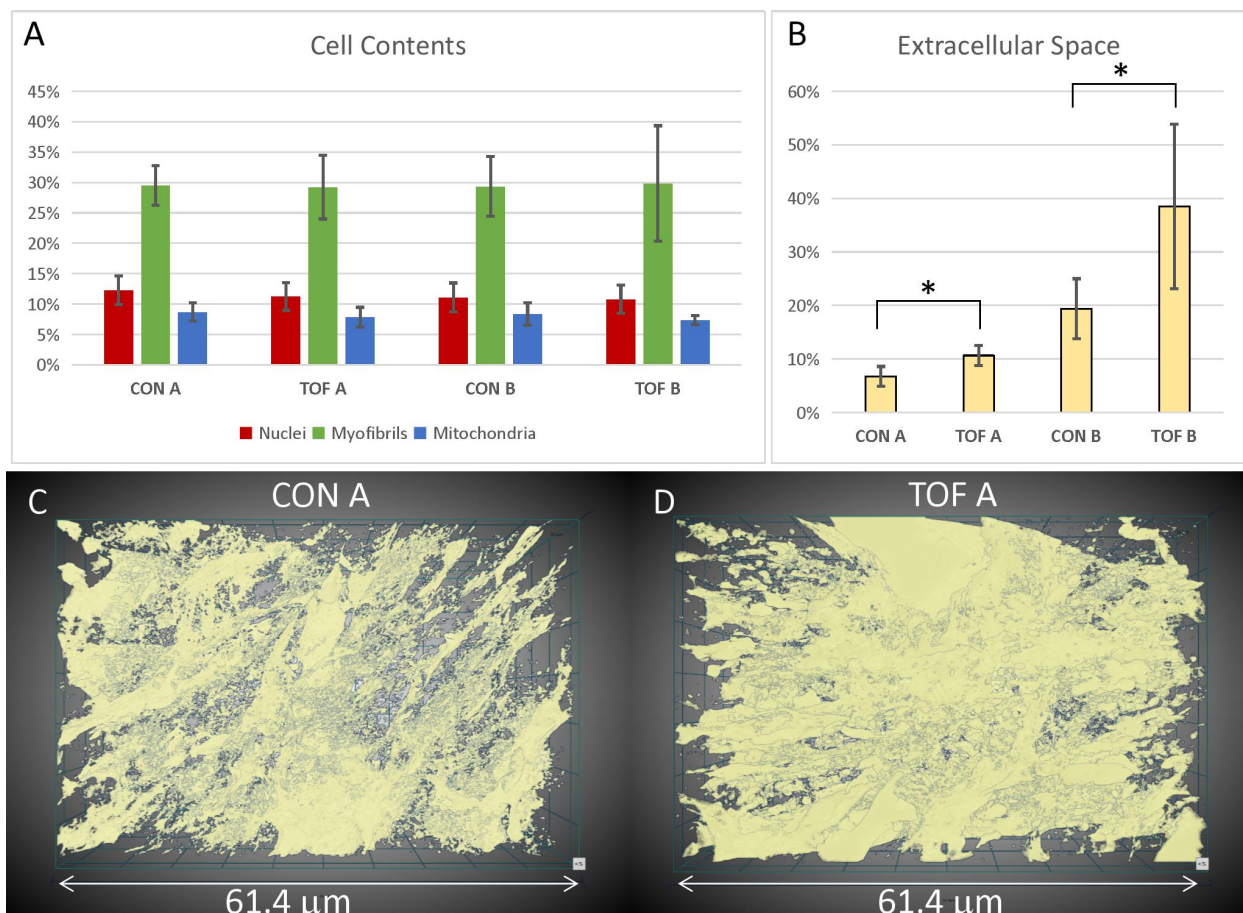
Image segmentation and quantification:

To better visualize and quantify the cardiac ultrastructure, we segmented (delineated) from SBF-SEM images the cell nuclei, myofibrils, mitochondria, and the extracellular space. To this end, we used a combination of deep learning algorithms and tools available on the Dragonfly 4.1 software (Object Research Systems, Quebec, Canada). When independently tested against carefully annotated images (2 each from control and TOF hearts, region A), the segmentation accuracy from the deep learning algorithm was at least 90% for myofibrils, 94% for mitochondria, and 98% for nuclei. Additional manual segmentation 'clean up' was thus required to improve the accuracy of organelle depictions. For quantification purposes, to control the accuracy of segmentations, we used subsets of the full SBF-SEM datasets by selecting images and regions within images from the complete dataset. From selected images and image regions, we quantified the percentage of the cell occupied by nuclei, myofibrils, and mitochondria. That is, we quantified selected organelle density within cells. We found that the density of nuclei, myofibrils and mitochondria was not significantly different between the control (CON) and TOF

Page | 10

221 hearts, nor between regions A and B (see **Figure 7A**). We also quantified the percentage of the
222 image that was occupied by extracellular space. We found that the TOF heart exhibited more
223 extracellular space than the CON heart in both regions A and B (see **Figure 7B**). This was also
224 consistent with a visual inspection of segmented images (see **Figure 7C**). In addition, for both
225 CON and TOF hearts, there was more extracellular space in region B than in region A ($p < 0.05$).

226

227

228 **Figure 7:** Segmentation and quantification of SBF-SEM images. Selected images ($n \geq 10$) from
229 the SBF-SEM image stacks acquired at regions A and B were carefully segmented and
230 quantified. **(A)** Percentage of myocardial cells occupied by nuclei, myofibrils and mitochondria in
231 two regions (A and B) of the control (CON) heart and TOF heart. **(B)** Percentage of the images
232 occupied by extracellular space. * indicates statistically significant differences ($p < 0.05$).
233 Although not marked, differences between regions A and B were also statistically significant. 3D
234 views of the segmented extracellular space in **(C)** control (CON) heart, region A; and **(D)** TOF
235 heart, region A.

236 Visualization of segmentations of the entire sub-ROIs from region A of the CON and TOF hearts
237 revealed a slightly different orientation of myocardial cells between samples (**Figure 8**).

238
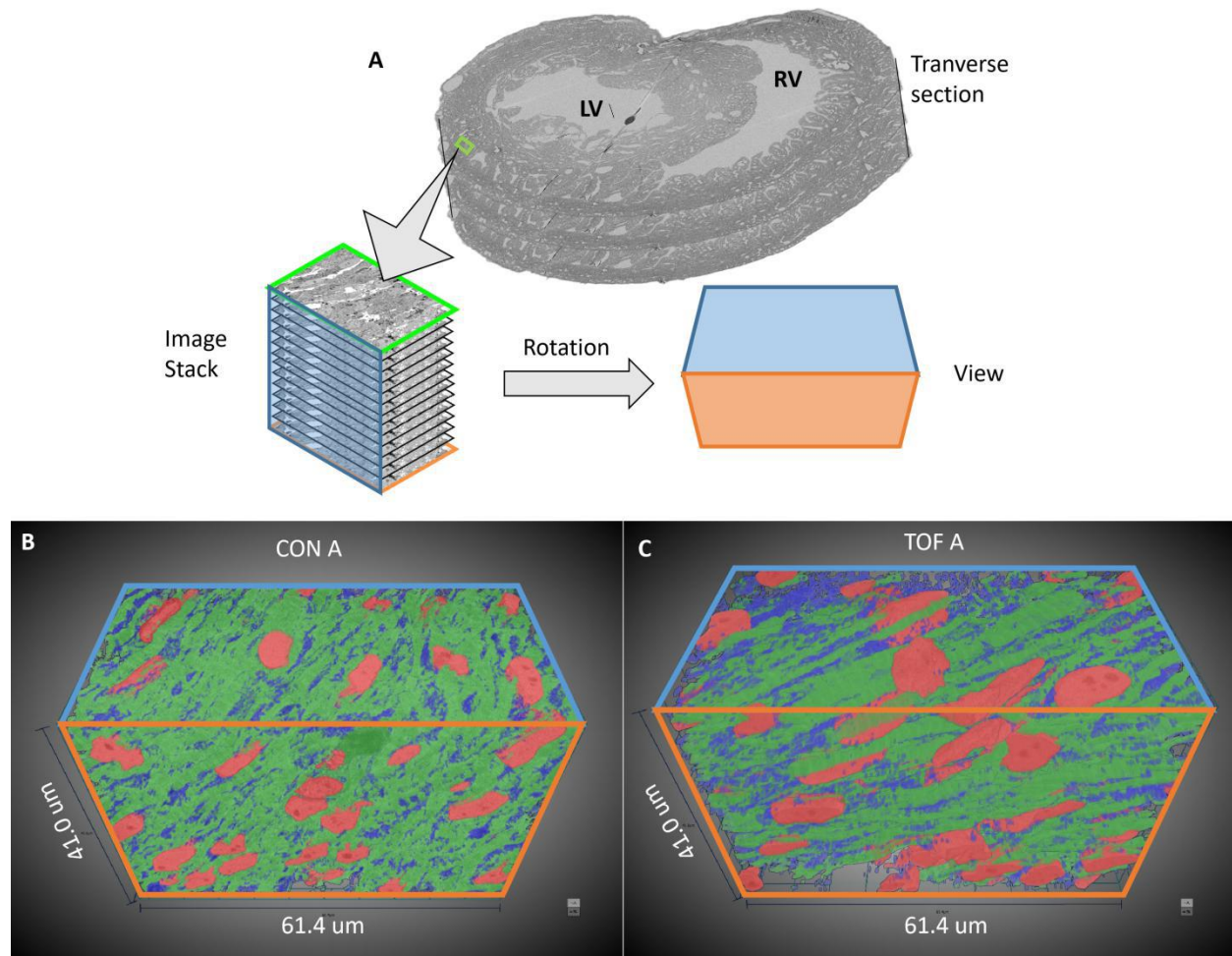
Figure 8: 3D visualization of SBF-SEM segmentations. **(A)** Sketch of image dataset acquisition, showing relative orientations. Green plane is the top image, orange plane is the bottom image (last image acquired), blue plane is approximately parallel to the heart wall. The sketch of the view shows the orientation of the planes as shown in **(B)** control (CON) heart and **(C)** TOF heart.

245 **Discussion**

246 Heart function relies on a multiscale, finely orchestrated contractile machinery. The heart
247 ultrastructural organization is needed for efficient heart pumping and is linked to the cell
248 metabolism [23-25]. Structural malformations in the chambers, valves or vessels of the heart,
249 together with disruptions to the organization or number of cardiac cells, and/or their
250 ultrastructure, can compromise the heart's ability to pump blood efficiently [8,10,13,26,27]. Anomalous
251 structural and ultrastructural architectures can be detrimental to the heart's capacity to adapt to
252 new conditions imposed by corrective surgeries or other therapies intended to repair structural
253 congenital heart defects. Thus, the organization of the heart at multiple scales needs to be
254 properly understood and accounted for in CHD treatment planning.

255 Heart walls contain myocardial cells, which are elongated, cylindrical-like muscle cells that are
256 aligned in patterns that optimize cardiac contractility [28,29]. Myocardial cells are about 50-150µm
257 long and 10-20µm thick (diameter), and in the heart are connected to each other forming a 3D
258 network [11]. More specifically, myocardial cells are organized in laminar sheets that exhibit
259 characteristic cell orientations (elliptical and transmural angles), which change over the heart
260 wall thickness and the cardiac cycle [11,30]. At the ultrastructural level, myocardial cells contain
261 contractile units, the myofibrils, which are supplied with energy (ATP) by the mitochondria
262 surrounding them. In a healthy, mature heart, myocardial nuclei have an ellipsoidal shape
263 aligned with the cell long axis; myofibrils are meticulously aligned and organized along the
264 myocardial cells; and mitochondria are densely packed around the myofibrils [16,29]. Other
265 organelles (such as lipid droplets and glycosomes) are organized around the cell myofibrils,
266 mitochondria and nuclei [31,32]. While this organization may vary significantly from individual to
267 individual, even in normal hearts, it ensures proper cardiac function. Multiscale studies of the
268 heart, spanning whole organ to ultrastructural details, can reveal subtle deficiencies in CHD
269 heart tissues, and relationships between abnormalities across spatial scales.

270 The correlative, multiscale imaging approach presented here was implemented and optimized in
271 a chicken embryo model of heart development and CHD [33]. Heart dimensions ranged from
272 approximately 5-6 mm long, 3-4 mm wide, and 250-700 µm wall thickness. We acquired images
273 of the whole embryonic heart using 3D micro-CT and of cardiac ultrastructure using 3D SBF-
274 SEM. Our multiscale imaging procedure achieved high-resolution images exhibiting both
275 microstructural and ultrastructural preservation, while protocol completion was achieved in
276 about 4 days, which is comparable to completion timings for much smaller samples [34]. Our
277 multiscale imaging methodology will enable studies of yet unknown tissue deficiencies in CHD.

278 Our protocol in relation to previous works

279 Researchers have used EM techniques, including SEM, for decades to visualize the
280 organization of organelles within cells [20,35]. In the heart, studies using EM have revealed the
281 ultrastructural architecture of mature myocardial cells [16,31], and elucidated the maturation of
282 myocardial ultrastructure during embryonic development [28,36,37]. A few studies, moreover, have
283 determined changes in ultrastructure due to pathophysiological conditions in the mature heart
284 [13,26,27]. Properly preparing samples for EM requires meticulous protocols that aim at preserving
285 the ultrastructure of the tissue under study (e.g. intact cell and nucleus membranes,

286   mitochondria and their crystae, myofibrils and z-disks, etc). Because the ultrastructural features
287   analyzed are at the nanometer scale, samples used for EM are typically very small (< 1mm^3),
288   which facilitates proper sample preparation. In preparing samples, portions of the heart are
289   typically excised, carefully prepared for imaging (fixed and stained) [14,38], and then imaged with
290   an EM modality [14,31]. Using this procedure, however, finding the ultrastructure associated with a
291   specific microscopic feature can be daunting. Moreover, in micro-dissecting tissue samples, the
292   myocardial organization within the heart may be lost [11]. Our methodology enables correlative
293   microscopy in a way that allows precise identification and mapping of portions of the heart to
294   their ultrastructure.

295   Whole animals and organs have been scanned with computed tomography (CT), a 3D x-ray
296   imaging modality, to determine the internal and external structure of organs, including the heart.
297   For small animal models, micro-CT, a high-resolution CT, is typically employed [33,39]. To enhance
298   contrast and thus resolution, prior to micro-CT imaging excised tissue samples are frequently
299   stained [33]. Preparing samples for micro-CT imaging requires good and uniform penetration of
300   the stain, intended to preserve and contrast the tissue microstructure (e.g., heart morphology,
301   heart chambers and valves). Micro-CT can then reveal subtle and overt malformations in the
302   heart and its microstructure [33]. For example, using micro-CT cardiac images it is possible to
303   visualize ventricular septal defects or translocations of the great arteries, but also wall and
304   septum thickness, and differentiate trabecular from compact myocardium [33]. The discrepancy in
305   the scale at which micro-CT and SBF-SEM are acquired introduces fundamental differences in
306   the requirements for sample preparation. Due to diverse fixation and staining protocols [33,40],
307   tissues prepared for micro-CT or other microstructural imaging (e.g. histology) cannot typically
308   be simultaneously processed for SBF-SEM (and other EM modalities), thereby restricting the
309   ability to analyze both the structural and ultrastructural characteristics within the same tissue
310   sample. Our correlative micro-CT/SBF-SEM procedure can reveal the sub-cellular architecture
311   associated with specific pathological or malformed regions of the heart found from micro-CT
312   images.

313   Applications combining micro-CT and EM technologies have recently begun to emerge, e.g. [41-43].
314   However, several challenges remain in applying these methods to correlative, multiscale
315   imaging of a relatively large organ like the heart (even the heart of a small animal). To achieve
316   both EM and micro-CT high-quality imaging of the same sample, existing protocols have
317   capitalized on heavy metal contrast in small tissue samples, which are fully processed prior to
318   EM and micro-CT imaging, e.g. [34,41]. However, achieving the uniform staining necessary for
319   optimal imaging with both micro-CT and SEM becomes progressively challenging with
320   increasing tissue sample size. This is mainly due to difficulties in achieving uniform and fast
321   fixation (that preserves the ultrastructure), and uniform stain penetration (both for post-fixation
322   purposes and to enhance contrast for SEM and micro-CT imaging). Modifications to the classic
323   ROTO protocols [19-21] for EM tissue preparation have been quite successful in achieving strong
324   and uniform staining of relatively large samples [44,45]. However, acceptable staining was typically
325   only up to a depth of 200 μm, and more recently 500 μm [19] in dense brain tissues. In an attempt
326   to stain whole brains for EM reconstruction of synapses, Mikula et al. developed the brain-wide
327   reduced-osmium staining with pyrogallol-mediated amplification (BROPA) protocol [46] for 3D
328   SBF-SEM (no other heavy metals were used). While the protocol is compatible with both micro-

329 CT and 3D SBF-SEM imaging, preparing a whole mouse brain (about 8-10 mm in diameter)
330 using BROPA required 2-3 months. A fast BROPA protocol (fBROPA) was later developed and
331 used to prepare whole brains from zebrafish in about 4 days [34]. Zebrafish brains, however, are
332 significantly smaller than mouse brains (diameter of 1.1 mm vs 8-10 mm, respectively). For our
333 hearts, we needed to achieve stain penetration of a relatively large sample (5-6mm long, 3-4
334 mm wide) and a fast preparation protocol was also desired. We found that preparing the heart
335 for SBF-SEM and stopping the protocol after initial ROTO staining, was compatible with micro-
336 CT and later SBF-SEM full sample processing and imaging. To our knowledge, this is the first
337 time that correlative micro-CT/SBF-SEM imaging is applied to the heart.

338 <u>Protocol implementation</u>

339 Sample preparation for SBF-SEM required strong, immediate fixation to preserve the
340 ultrastructure of the heart tissue. We used a modified Karnovsky's fixative with equal parts
341 glutaraldehyde and paraformaldehyde: The paraformaldehyde rapidly penetrated and
342 temporarily stabilized the tissue, and the slower-penetrating glutaraldehyde, a superior cross-
343 linker, more permanently preserved the tissue sample [35]. An obvious difficulty was to achieve
344 uniform fixation of the whole heart sample. Homogenous fixation was achieved by perfusing
345 fixative into the heart prior to excision and then promptly immersing the heart in fixative after
346 excision, allowing the fixative to simultaneously penetrate the heart through the tissue's internal
347 and external surfaces. The hearts were then post-fixed with osmium tetroxide, a lipid cross-
348 linker, which fully stabilized membrane structures while enhancing contrast for micro-CT and
349 SBF-SEM imaging. For our heart samples, we could achieve uniform stain penetration using a
350 variation of the ROTO protocol with extended staining timing (about 30% increase; see
351 Methods). The extended timing was sufficient for our hearts, even considering small size
352 variations. We expect, however, that further time increases would apply to larger heart samples
353 (for instance if we image embryos at a more advanced developmental stage, or other species
354 are considered). For the chick embryos studied here, sample preparation after ROTO was
355 adequate for micro-CT imaging of the whole heart (see **Figure 2**).

356 For 3D SBF-SEM images, heart samples were further stained with a combination of heavy
357 metals. This is because SEM images are acquired via the detection of secondary and
358 backscattered electrons that are emitted as the tissue is scanned with a high energy beam of
359 primary electrons [47]. Soft biological tissues, like the heart muscle, yield few backscattered
360 electrons and need to be stained with heavy metals, which readily produce secondary and
361 backscattered electrons. Heavy metal stains interact with specific ultrastructural components,
362 and therefore combinations of stains are frequently used in a single sample. The application of
363 osmium tetroxide, used in ROTO protocols, served as the first application of a heavy metal stain
364 in the SBF-SEM preparation. The osmium tetroxide, which interacts with lipids in membranes
365 and vesicles, both post-fixed and stained tissues. Further staining with uranyl acetate stained
366 lipids and proteins, and lead aspartate stained proteins and glycogens. Together, these heavy
367 metal stains fully preserved and contrasted ultrastructural details, as evidenced by high-
368 resolution SBF-SEM images (see **Fig. 5**).

369 For whole-heart samples, we found that staining with uranyl acetate and lead aspartate
370 rendered resin-embedded hearts opaque to micro-CT imaging (data not shown). Our multiscale
371 multimodality imaging procedure overcame these difficulties by performing micro-CT imaging
372 after ROTO (see above) but prior to the lead and uranium staining steps, such that correlative
373 3D micro-CT and 3D SBF-SEM could be implemented. This initial modified ROTO post-fixing
374 and staining provided tissue contrast for micro-CT while also ensuring that the sample was
375 preserved and stabilized before final SBF-SEM sample preparation and imaging (see **Figure 1**).
376 In addition, it enabled screening, storing and selection of hearts before final SBF-SEM
377 processing. This feature of our multiscale approach is advantageous for several reasons. At this
378 early processing point, hearts could be stored for relatively long periods (at least 2 weeks, but
379 potentially months/years) before further processing. This allows researchers to prepare and
380 screen by micro-CT a large number of hearts, and then select only those hearts of interest (e.g.
381 with a specific malformation) for further analysis with SBF-SEM. Not only does this approach
382 permit banking of samples, but it also saves considerable time and resources by avoiding full
383 sample preparation of hearts that are not useful. This is important for our application, in which at
384 most 60% of treated hearts develop structural malformations, and the nature and severity of
385 defects vary among individual hearts. Since we cannot accurately classify malformations until
386 they are scanned with micro-CT, being able to use the micro-CT as both a screening tool and as
387 a navigational tool for later correlative microscopy is invaluable to CHD studies.

388 Due to the size of the hearts and slow diffusion (penetration) of heavy metals into the tissue,
389 achieving uniform staining during further SBF-SEM tissue processing was not straightforward.
390 Initial iterations of the procedure (data not shown) resulted in a strong gradient of staining into
391 the heart tissue, a manifestation of poor stain penetration [34,46]. Application of microwave steps to
392 enhance diffusion was not helpful, although perhaps optimizations of those steps could achieve
393 improved results. We found, however, that following a Renovo Neural, Inc. protocol (see
394 Methods) after ROTO and before embedding the sample in a resin capsule allowed the samples
395 to achieve homogeneous staining. Uniform stain penetration throughout the heart, was apparent
396 from semithin transverse sectional images of the heart and low-resolution images of ROIs (see
397 **Figure 4**). The uniform contrast and resolution of ultrastructural details provided further
398 evidence of uniform staining and proper tissue fixation (see **Figure 5**).

399 While the focus of this study was to demonstrate homogeneous staining and fixation, our
400 procedure enables correlative microscopy. One way to achieve accurate localization of
401 ultrastructures within the heart structure, is to register semithin transverse sections to micro-CT
402 images, and then SBF-SEM images to the semithin images (as done in **Figure 4**). Because
403 sectioning of samples for SBF-SEM imaging is done after micro-CT images are acquired,
404 sectioning is guided by the images of the whole heart, facilitating the selection of regions of
405 interest. Registration can then be performed among the images themselves. This could be done
406 directly, or by adding fiduciary markers in the resin/heart to facilitate image alignment. Our
407 procedure allows imaging of ultrastructure at several regions of interest within the heart,
408 enabling extensive ultrastructural mapping.

409 <u>Comparison of control and TOF hearts and limitations of this study</u>

410   We further explored some possible analysis and quantification strategies enabled by our
411   procedure. We acknowledge that any results from this study are very preliminary, and any
412   statistically significant differences show here pertain only to the two hearts studied. Analysis of
413   more heart samples is needed to reach conclusions applicable to CHD. In the future, a
414   combination of segmentation, quantification and other refined methods to interrogate the images
415   (at the microstructural and ultrastructural levels) will elucidate similarities and differences
416   between normal and malformed hearts, possibly informing therapeutic treatment strategies.

417   Micro-CT images reveal the microstructural characteristics of hearts. Not only could we classify
418   the hearts based on phenotype (normal vs TOF), but (while not reported here) cardiac
419   characteristics, such as heart size and wall thickness could be visualized and quantified. For
420   example, it was noted from our analysis that the RV of the TOF heart exhibited a larger volume
421   and thinner ventricular walls than that of the control (CON) heart examined here (see **Figure 3**).
422   During fetal life, the lungs are not functional, and blood to the lungs is shunted to the systemic
423   circulation through the ductus arteriosus [48] (a pair of ducti in chick [49]). The RV hypertrophy
424   characteristic of TOF, develops over time after the baby is born [50]. RV hypertrophy, therefore,
425   may not be present at the fetal stages of heart development examined in this study and was not
426   observed in our TOF heart. In the future, it would be interesting to determine whether the trait
427   observed in this study is preserved among TOF fetal hearts, and if so under which conditions
428   and how it affects the RV wall ultrastructure (not examined here). Such study, however, requires
429   a larger number of heart samples, and is outside of the scope of this paper.

430   Another difference between the two hearts, was that the ventricles of the TOF heart exhibited
431   less dense tissue and a more extended trabecular architecture compared with the control heart.
432   This is consistent with reduced myocardial compaction in TOF [51-53]. The heart trabeculae is
433   characterized as a "spongy" or porous tissue that develops inside the heart ventricles, and in
434   our samples was evident from semithin transverse heart sections (**Figure 4**), but could also be
435   approximately quantified as the extracellular portion of the images (**Figure 7**). It has been
436   shown that the heart trabecular architecture is sensitive to blood flow conditions during
437   development [54], and thus a disrupted trabecular architecture may be a characteristic of TOF
438   hearts due to their anomalous flow characteristics during fetal stages [18]. However, the
439   trabecular and myocardial architecture can also exhibit variations from heart to heart [11],
440   therefore further analysis with a larger sample size is required before we can make conclusions
441   related to TOF.

442   We noticed differences in SBF-SEM image sharpness, which are attributable to excessive
443   'charging' (accumulation of static charge on a sample's surface) when scanning the TOF heart
444   (**Figure** 5). The increased charging in our TOF heart is linked to its trabeculation, which features
445   larger and more numerous void regions filled with free resin. To address this problem during
446   imaging, we slightly shortened the dwell time when acquiring SBF-SEM images from the TOF
447   sample. In the future, we could embed silver particles in the resin to increase sample
448   conductivity and enhance image quality [34]. Nevertheless, the image quality of both the TOF and
449   the control hearts was sufficient to appreciate ultrastructural details (**Figure 5**).

450 While 2D EM images have been invaluable in deciphering ultrastructural features of myocardial
451 cells and tissues, 3D images can unravel more details in the spatial organization of the
452 ultrastructural architecture [16,26]. As an example, segmentation and visualization of the 3D data
453 revealed that myofibril alignment was slightly different between our TOF and control hearts
454 (**Figure 8**). This is perhaps because the ROIs from the two hearts are not exactly corresponding,
455 or due to the more extended trabecular architecture of the TOF heart, and warrants further
456 investigation. For myocardial alignment quantification, it is also important to arrest the heart
457 consistently (in diastole as done here, or systole) as myocardial cell orientation changes over
458 the cardiac cycle [12,30]. 3D SBF-SEM images also revealed a greater proportion of endocardial
459 cells in TOF heart tissues than in control tissues, such that volumetric studies not focusing on
460 myocardial cells show reductions in the myofibril density of the TOF heart (data not shown).
461 When the analysis is focused exclusively on myocardial cells, however, we could not find any
462 differences in the density of myofibrils or mitochondria (**Figure 7**). While outside the scope of
463 this paper, future studies should focus on elucidating ultrastructural cardiac differences in
464 animal models of CHD as such differences can impact the lives of children and adults with
465 congenital heart defects. Our proposed multiscale imaging methodology will certainly enable
466 such studies.

467

468 **Conclusions**

469 Our correlative, multiscale imaging procedure allowed us to acquire detailed micro-CT images
470 of an entire embryonic chicken heart (see **Figure 2**), followed by ultrastructural 3D SBF-SEM
471 images from the same heart (see **Figures 4** and **5**). Our approach thus enables detailed
472 analysis of both whole heart morphology and ultrastructural architecture, allowing determination
473 of cardiac malformations and subcellular organization within specific regions of the heart. This is
474 important when studying CHDs, as each malformation phenotype may be different and therefore
475 may need to be analyzed separately to fully appreciate multiscale effects and to understand
476 how phenotypes affect cardiac architecture at disparate levels. The multiscale imaging
477 approach presented here will enable studies to determine how cardiac anomalies, even when
478 repaired, could subsequently lead to increased cardiac dysfunction and heart failure. For
479 patients with CHD, such studies may reveal associated pathologies in cardiac tissues that, if not
480 properly treated, may have devastating implications for survival and long term cardiac health.

481 While our developed multiscale approach was implemented and optimized using embryonic
482 chicken hearts, we expect it will be straightforward to adapt it for use in mouse and other small
483 animal models of cardiac malformations. It will be advantageous to use complementary models,
484 as typically genetic insults are studied using mouse models, while environmental perturbations
485 are studied using avian models. Heart dimensions in those species (mouse and chick) are very
486 similar, and we anticipate that tissue processing will not differ significantly. Slight increases in
487 heart size may just require an increase in protocol staining times. Extending the approach to
488 different species and models of congenital heart disease will enable us to understand in detail
489 the similarities and differences between cardiac defects, and the underpinnings of
490 malformations that result from genetic and environmental insults.

Methods

Ethical Considerations:

Our research used chicken embryos. According to the US National Institutes of Health (NIH) Office of Laboratory Animal Welfare (_ILAR News_ 1991; 33(4):68-70), the NIH's "Office for Protection from Research Risks has interpreted 'live vertebrate animal' to apply to avians only after hatching." Our Institutional animal care and use committee (IACUC) follows NIH interpretation. Therefore, chicken embryos are not considered animals and our research did not require approval. Incubator logs in the lab were monitored daily to ensure there were no eggs near the hatching time of 21 incubation days. Nevertheless, we used the minimum possible number of embryos to achieve our goals.

Generation of cardiac defects:

Our multiscale approach was implemented and optimized using fully formed embryonic chicken hearts (heart length ~5-6mm), and applied to a chick animal model of congenital heart disease. Chicken embryos were prepared as described previously [33]. Briefly, fertilized white Leghorn chicken eggs were incubated blunt end up at 38°C and 80% humidity for approximately 3 days (to Hamburger and Hamilton (HH) stage HH18 [55]). Control and treatment interventions were then performed as described below and the embryos were re-incubated for an additional 9 days (to HH38, when the heart has four chambers and valves). Two embryonic hearts were included in this study: 1) a control, normal heart; and 2) a malformed heart with tetralogy of Fallot (TOF). TOF was achieved by performing outflow tract banding (OTB) at HH18, wherein a 10-0 nylon suture was passed under the mid-section of the heart outflow tract and tied in a knot (band tightness 38%). The band was removed from the outflow tract ~24 hours after placement (HH24), and then the embryo was allowed to develop to HH38. The control heart was obtained by passing a 10-0 nylon suture under the heart outflow tract without knotting it, and subsequently allowing the embryo to develop to HH38. Embryo hearts were collected at HH38 for multiscale imaging.

Homogenous fixation of whole hearts:

At HH38, embryonic whole hearts were excised and fixed as follows. The chest cavity was opened and the pericardial sac around the heart gently removed with forceps. Each heart was arrested by injecting 500 µL of chick ringer solution containing 60 mM KCl, 0.5 mM verapamil, and 0.5 mM EGTA [56] into the left ventricle through the heart's apex. Hearts were then immediately perfused with ~2 mL of ice-cold (0˚C) modified Karnovsky's fixative (2.5% Glutaraldehyde and 2.5% PFA in PBS (pH 7.4)) through the same injection site. All perfusions were performed with a 21 gauge needle. A transfer pipette was used to quickly apply ~1 mL of fixative to the heart's exterior to ensure uniform fixation of the heart tissue. Next, the heart great vessels were cut with small spring scissors and hearts were placed in 1.5 mL fixative and stored at 4°C until further processing.

Cardiac processing enabling micro-CT imaging:

529   In order to enable both whole-heart micro-CT imaging and subsequent SBF-SEM imaging of
530   regions of interest (ROIs), we processed fixed hearts for micro-CT using the initial portion of a
531   Renovo Neural, Inc (Cleveland, USA) protocol [38] designed for SBF-SEM imaging (see **Figure 1**,
532   **Step 1**). Each heart was placed in a 5 mL glass scintillation vial and we used 3 mL of solution
533   per vial for each incubation/wash. First, the fixed hearts were washed in 0.1M Sodium
534   Cacodylate (pH 7.4) for 20 minutes with 4 exchanges of fresh buffer. Next, the hearts were
535   incubated in 0.1% (w/v) of tannic acid in 0.1M Sodium Cacodylate (pH 7.4) for 15 minutes at
536   room temperature. Samples were then washed in 0.1M Sodium Cacodylate (pH 7.4) for 20
537   minutes with 4 exchanges of fresh buffer. Since the reducing agents used in subsequent steps
538   (modified ROTO protocol) were light-sensitive, the sample vials were covered in aluminum foil
539   from this point on. The whole hearts were post-fixed in 2% (v/v) Osmium Tetroxide (OsO_4) and
540   1.5% (w/v) Potassium Ferricyanide ($K_3[Fe(CN)_6]$) in distilled water (dH_2O) for 2 hours at room
541   temperature on a rotating platform. The samples were then extensively washed in dH_2O for 20
542   minutes with 4 exchanges of fresh dH_2O. Next, the samples were immersed in 0.1% (w/v)
543   Thiocarbohydrazide (TCH) solution in dH_2O, placed in an oven, and incubated for 40 minutes at
544   60°C. This step was followed by another 4 exchanges of fresh dH_2O over 20 minutes. Samples
545   were then immersed in a 2 % (v/v) OsO_4 solution in dH_2O for 2 hours at room temperature on a
546   rotating platform. Finally, the hearts were washed extensively in dH_2O over 20 minutes with 4
547   exchanges of fresh water. Each heart was stored in dH_2O at 4°C until imaged by micro-CT. This
548   preparation provided excellent contrast for micro-CT scans (see Results).

549   Micro-CT images of whole hearts were acquired to assess the cardiac structure. We acquired
550   high-resolution (~10 μm) 3D scans of each heart using a Caliper Quantum FX Micro-CT system
551   (Perkin-Elmer, CLS140083) with 10 mm field of view, 140 μA current, 90 kV voltage, and a scan
552   time of 3 minutes. We used the Amira 6.0 software platform (FEI Company) to visualize these
553   scans and identify cardiac defects. Hearts were then stored in double distilled water at 4°C until
554   further processing. Please note that at this step in the processing (cardiac tissues fixed and
555   post-fixed with OsO_4) water does not damage the tissues.

556   <u>Subsequent cardiac tissue processing enabling 3D SBF-SEM imaging:</u>

557   After whole hearts were imaged with micro-CT, sample preparation of selected hearts for 3D
558   SBF-SEM imaging was finished (see **Figure 1**; **Step 2**), following the Renovo Neural, Inc.
559   protocol. In large samples, like the whole hearts described in this manuscript, it is necessary to
560   extend most of the staining steps. Failure to extend the timing of staining resulted in a
561   heterogenous stain distribution throughout the tissue (in our early iterations of the procedure). In
562   our final, optimized procedure, we incubated the samples in 1% (w/v) aqueous uranyl acetate
563   for 24 hours at 4°C, after which they were washed in dH_2O for 30 minutes with 6 exchanges of
564   fresh dH_2O. We then incubated the samples in lead aspartate for 30 minutes at 60°C. The
565   samples were then extensively washed in dH_2O for 20 minutes with 4 exchanges of dH_2O.
566   Dehydration steps were done in a series of acetone-dH_2O mixtures (50, 75, 85, 95 and 100%);
567   each step was repeated twice for 5 minutes at room temperature. The whole heart sample was
568   then embedded in an epoxy (Epon 812) resin for further manipulation and SBF-SEM sample
569   preparation. The first infiltration step was done for 1 hour at room temperature in a mixture of
570   1:1 (v/v) acetone:epon followed by a 1:3 (v/v) acetone:epon incubation for 1 hour at room

571 temperature. The hearts were subsequently incubated overnight in pure (100%) epon on a
572 rotating platform. The following day the epoxy solution was exchanged 4 times, each time with
573 30 minutes incubation steps at room temperature. Samples were polymerized at 60°C for 48
574 hours in a conventional oven, leading to a whole heart sample embedded in an Epon block.

575 Selection of regions of interest (ROIs) and SBF-SEM image acquisition:

576 Using the micro-CT images as reference, the Epon-embedded heart blocks were sectioned to
577 reach a selected short axis (transverse) section using a diamond-wire jewelry saw. For this
578 study we selected the mid cardiac transverse section, at a plane where the heart is wider (the
579 equatorial plane). After this step, a semithin section (250 nm) was obtained using an
580 ultramicrotome and mounted on a silicon chip previously glow discharged for 1 minute at 15 mA
581 (PELCO easyGlow, Ted Pella). Semithin section images were used to confirm the area of
582 interest as well as to check for both the ultrastructural quality of the sample and the success of
583 the staining procedure (see **Figure 1**; **Step 2**). This step is crucial since the SBF-SEM imaging
584 requires samples with extremely good contrast. Semithin sections were imaged on a Teneo
585 Volume Scope in low vacuum mode using a VS-DBS backscattered electron detector and the
586 MAPS software (FEI Company). Imaging conditions used were 2.5 kV and 0.2 mA, dwell 3-5 μs.
587 In some cases, the samples imaged using this method needed to be coated with a thin (5-8 nm)
588 layer of carbon to minimize charging artifacts induced by the electron beam.

589 The same diamond-wire jewelry saw was then utilized to generate a slab (~1.5 mm) from the
590 sample (see **Figure 1**; **Step 3**). The slabs were sectioned into smaller ROIs, which were
591 subsequently mounted on Microtome stub SEM pins (Agar Scientific 61092450) using H20E
592 Epo-Tek silver epoxy (Ted Pella 16014) and cured overnight at 60°C in a conventional oven.
593 The resulting small blocks were then trimmed using a Trim90 diamond knife (Diatome) to
594 generate a pillar of 500x500 μm^2. The block was then coated with 20 nm of gold using a Leica
595 ACE 600 unit.

596 In the last step of our multiscale imaging procedure, 3D SBF-SEM images of sub-ROIs selected
597 from the mounted sample were acquired (see **Figure 1**; **Step 4**). 3D image acquisition was
598 done on a Teneo Volume Scope SBF-SEM in low vacuum mode (50 Pa) using a VS-DBS
599 backscattered detector. Images were acquired at a lateral resolution of 10 nm/pixel and image
600 sets included 800-1000 serial sections (with each section thickness measuring 40 nm in the z
601 axis). SBF-SEM data sets were approximately 40 μm × 60 μm × 32-40 μm.

602 Image Analysis and Segmentation:

603 All registration, of SBF-SEM data was performed with Amira 6.0 (FEI Company). First, complete
604 image stacks (800-1000 slices) from each ROI and sub-ROIs were automatically aligned to
605 generate a continuous 3D volume. Next, a non-local means filter was applied to every 2D slice
606 in order to improve the signal-to-noise ratio. Due to slight differences in the intrinsic properties of
607 the tissue, sections from the TOF heart appeared slightly lighter compared to the control heart.
608 We adjusted the intensity of the TOF sections during post-processing to match that of the
609 control heart.

610   To better appreciate ultrastructural differences between the two hearts, we used Dragonfly 4.1
611   software (Object Research Systems, Quebec, Canada) to segment and quantify SBF-SEM
612   images. We segmented: cell nuclei, mitochondria, myofibrils and the extracellular space (this
613   later one to allow quantification of relative organelle volume within cells). The segmentation
614   used a combination of tools in Dragonfly, including deep learning algorithms. Briefly, we
615   employed a six-level U-Net deep learning model [57] implemented in Dragonfly to perform an
616   initial segmentation of nuclei, mitochondria, and myofibrils within imaged cells. Training sets
617   required for the deep learning model were obtained initially through manual segmentations of a
618   few selected images from the image stacks. The training set was later augmented by applying
619   the segmentation deep learning algorithms to other (selected) images from the set, follow by
620   thorough manual cleaning. For each training session, the model was run for 50 epochs with a
621   patch size of 128 pixels. Dragonfly automatically divides the training sets into training and
622   validation regions, so that training (and further inclusion of training images) continued until the
623   reported accuracy (from validation regions) was > 98% with a loss < 0.06. Images were then
624   segmented with the trained model, and segmentations further refined both using Dragonfly
625   automated tools, such as morphological operations, and manual clean up using painter tools
626   available in Dragonfly. Unlike organelles, the extracellular space was easily recognized by
627   intensity levels, and thus simply segmented based on its intensity, followed by clean up using
628   both automatic and manual tools in Dragonfly.

629   For visualization purposes, we segmented a whole dataset from the control heart and an
630   approximately corresponding dataset from the TOF heart (region A, **Figure 8**). The total volume
631   of the dataset was 40x60x32 μm^3. For quantification purposes, we segmented and further
632   curated smaller portions of the data sets from two corresponding regions of the control and the
633   TOF hearts (regions A and B). Quantifications of extracellular space and nuclei were done from
634   17 evenly spaced images from the 800 image datasets of region A; and 21 evenly spaced
635   images from the 1000 image datasets of region B (thus every 50th image was used for these
636   segmentations). For quantification of mitochondria and myofibrils, we cropped images (n ≥ 10)
637   so that we could focus on smaller regions, allowing us to manually improve the accuracy of
638   segmentations in a more tractable manner and focusing on myocardial regions.

639   Quantifications were performed based on segmented images. We quantified, from each image
640   or image portion, the total surface area (S_T), and the surface area occupied by extracellular
641   space (S_E), nuclei (S_N), mitochondria (S_{Mit}) and myofibrils (S_{Myo}). We then computed the fraction
642   of the total surface area occupied by the extracellular space (S_E/S_T); and the fraction of the cell
643   occupied by organelles (nuclei, mitochondria and myofibrils), computed as the ratio of organelle
644   surface (S_i, with i = N, Mit, Myo) to the cell surface ($S_i/(S_T - S_E)$). Because quantifications were
645   performed from different portions (n ≥ 10) of the dataset, average and standard deviations were
646   calculated to represent quantifications for the dataset (control or TOF hearts, regions A and B).
647   We then employed a one tail T-test to compare quantifications among datasets, with $p < 0.05$
648   indicating significant differences.

649

650

Acknowledgements

Author Contributions

G.R. prepared the samples, acquired micro-CT images, and analyzed micro-CT and EM images. C.S.L and J.L.R. optimized the sample preparation protocols and acquired the EM images. I.F. segmented and quantified the SBF-SEM images. S.D. segmented micro-CT images for comparison. K.C. analyzed images and assisted G.R. with figures. A.M and K.T. analyzed the quality of images and helped with biological image interpretation. S.R. conceived the project, and wrote the first draft of the manuscript. All authors reviewed and edited the manuscript.

Competing Interests

The authors declare no competing interests.

Data Availability

Data, including micro-CT and SBF-SEM images, will be available to researchers upon request. Protocols employed are fully disclosed and detailed in the manuscript methods section.

References

1   Gilboa, S. M., Salemi, J. L., Nembhard, W. N., Fixler, D. E. & Correa, A. Mortality resulting from congenital heart disease among children and adults in the United States, 1999 to 2006. *Circulation* **122**, 2254-2263, doi:10.1161/CIRCULATIONAHA.110.947002 (2010).

2   van der Linde, D. *et al.* Birth Prevalence of Congenital Heart Disease WorldwideA Systematic Review and Meta-Analysis. *Journal of the American College of Cardiology* **58**, 2241-2247, doi:10.1016/j.jacc.2011.08.025 (2011).

3   Czosek, R. J. & Anderson, J. B. Congenital heart disease and the cost of mortality. *Open Heart* **3**, e000448, doi:10.1136/openhrt-2016-000448 (2016).

4   Gilljam, T. *et al.* Development of heart failure in young patients with congenital heart disease: a nation-wide cohort study. *Open heart* **6**, e000858-e000858, doi:10.1136/openhrt-2018-000858 (2019).

5   Oster, M. E. *et al.* Temporal Trends in Survival Among Infants With Critical Congenital Heart Defects. *Pediatrics* **131**, e1502-e1508, doi:10.1542/peds.2012-3435 (2013).

6   Stout, K. K. *et al.* Chronic Heart Failure in Congenital Heart Disease. *A Scientific Statement From the American Heart Association*, doi:10.1161/cir.0000000000000352 (2016).

7   Sugimoto, M. *et al.* Cardiac biomarkers in children with congenital heart disease. **11**, 309-315, doi:10.1007/s12519-015-0039-x (2015).

8   Garcia-Canadilla, P. *et al.* Myoarchitectural disarray of hypertrophic cardiomyopathy begins pre-birth. *Journal of Anatomy* **0**, doi:10.1111/joa.13058 (2019).

9   Stephenson, R. S. *et al.* High-Resolution Contrast-Enhanced Micro-Computed Tomography to Identify the Cardiac Conduction System in Congenitally Malformed Hearts. *Valuable Insight From a Hospital Archive* **11**, 1706-1712, doi:10.1016/j.jcmg.2018.05.016 (2018).

10   Garcia-Canadilla, P. *et al.* Complex Congenital Heart Disease Associated With Disordered Myocardial Architecture in a Midtrimester Human Fetus. *Circulation: Cardiovascular Imaging* **11**, e007753, doi:doi:10.1161/CIRCIMAGING.118.007753 (2018).

11   Gilbert, S. H., Benson, A. P., Li, P. & Holden, A. V. Regional localisation of left ventricular sheet structure: integration with current models of cardiac fibre, sheet and band structure☆. *European Journal of Cardio-Thoracic Surgery* **32**, 231-249, doi:10.1016/j.ejcts.2007.03.032 (2007).

12   Omann, C. *et al.* Resolving the natural myocardial remodelling brought upon by cardiac contraction; a porcine ex-vivo cardiovascular magnetic resonance study of the left and right ventricle. *Journal of Cardiovascular Magnetic Resonance* **21**, 35, doi:10.1186/s12968-019-0547-2 (2019).

13   Sanchez-Quintana, D., Climent, V., Ho, S. Y. & Anderson, R. H. Myoarchitecture and connective tissue in hearts with tricuspid atresia. *Heart* **81**, 182-191, doi:10.1136/hrt.81.2.182 (1999).

14   Rennie, M. Y., Gahan, C. G., López, C. S., Thornburg, K. L. & Rugonyi, S. 3D Imaging of the Early Embryonic Chicken Heart with Focused Ion Beam Scanning Electron Microscopy. *Microscopy and Microanalysis* **20**, 1111-1119, doi:doi:10.1017/S1431927614000828 (2014).

15   Midgett, M., López, C. S., David, L., Maloyan, A. & Rugonyi, S. Increased Hemodynamic Load in Early Embryonic Stages Alters Myofibril and Mitochondrial Organization in the Myocardium. *Frontiers in Physiology* **8**, doi:10.3389/fphys.2017.00631 (2017).

16   Hussain, A. *et al.* An Automated Workflow for Segmenting Single Adult Cardiac Cells from Large-Volume Serial Block-Face Scanning Electron Microscopy Data. *bioRxiv*, 242701, doi:10.1101/242701 (2018).

17   Bailliard, F. & Anderson, R. H. Tetralogy of Fallot. *Orphanet journal of rare diseases* **4**, 2-2, doi:10.1186/1750-1172-4-2 (2009).

729 18   Wiputra, H. *et al.* Human fetal hearts with tetralogy of Fallot have altered fluid dynamics and
730   forces. *American Journal of Physiology-Heart and Circulatory Physiology* **315**, H1649-H1659,
731   doi:10.1152/ajpheart.00235.2018 (2018).
732 19   Hua, Y., Laserstein, P. & Helmstaedter, M. Large-volume en-bloc staining for electron
733   microscopy-based connectomics. *Nature Communications* **6**, 7923, doi:10.1038/ncomms8923
734   (2015).
735 20   Malick, L. E., Wilson, R. B. & Stetson, D. Modified Thiocarbohydrazide Procedure for Scanning
736   Electron Microscopy: Routine use for Normal, Pathological, or Experimental Tissues. *Stain*
737   *Technology* **50**, 265-269, doi:10.3109/10520297509117069 (1975).
738 21   Willingham, M. C. & Rutherford, A. V. The use of osmium-thiocarbohydrazide-osmium (OTO)
739   and ferrocyanide-reduced osmium methods to enhance membrane contrast and preservation in
740   cultured cells. *Journal of Histochemistry & Cytochemistry* **32**, 455-460,
741   doi:10.1177/32.4.6323574 (1984).
742 22   Reading, D. W. & Oza, U. Unilateral absence of a pulmonary artery: a rare disorder with variable
743   presentation. *Proceedings (Baylor University. Medical Center)* **25**, 115-118 (2012).
744 23   Spotnitz, H., Sonnenblick, E. & Spiro, D. Relation of ultrastructure to function in the intact heart:
745   Sarcomere structure relative to pressure volume curves of intact left ventricles of dog and cat.
746   *Circulation Research* **XVIII**, 49-66 (1966).
747 24   Feuvray, D. in *Advances in Myocardiology: Volume 4* (eds E. Chazov, V. Saks, & G. Rona) 441-
748   448 (Springer US, 1983).
749 25   Sahli Costabal, F. *et al.* Multiscale characterization of heart failure. *Acta Biomaterialia* **86**, 66-76,
750   doi:https://doi.org/10.1016/j.actbio.2018.12.053 (2019).
751 26   Pinali, C. *et al.* Three-dimensional structure of the intercalated disc reveals plicate domain and
752   gap junction remodeling in heart failure. *Biophysical journal* **108**, 498-507,
753   doi:10.1016/j.bpj.2014.12.001 (2015).
754 27   Holzem, K. M. *et al.* Mitochondrial structure and function are not different between nonfailing
755   donor and end-stage failing human hearts. *The FASEB Journal* **30**, 2698-2707,
756   doi:10.1096/fj.201500118R (2016).
757 28   Fischman, D. A. An Electron Microscope Study of Myofibril Formation in Embryonic Chick
758   Skeletal Muscle. *The Journal of Cell Biology* **32**, 557-575, doi:10.1083/jcb.32.3.557 (1967).
759 29   Brook, W. H., Connell, S., Cannata, J., Maloney, J. E. & Walker, A. M. Ultrastructure of the
760   myocardium during development from early fetal life to adult life in sheep. *Journal of anatomy*
761   **137 (Pt 4)**, 729-741 (1983).
762 30   Sonnenblick, E. H., Ross, J., Covell, J. W., Spotnitz, H. M. & Spiro, D. The Ultrastructure of the
763   Heart in Systole and Diastole. *Circulation Research* **21**, 423-431,
764   doi:doi:10.1161/01.RES.21.4.423 (1967).
765 31   Pinali, C. & Kitmitto, A. Serial block face scanning electron microscopy for the study of cardiac
766   muscle ultrastructure at nanoscale resolutions. *Journal of Molecular and Cellular Cardiology* **76**,
767   1-11, doi:10.1016/j.yjmcc.2014.08.010 (2014).
768 32   Pinali, C., Bennett, H., Davenport, J. B., Trafford, A. W. & Kitmitto, A. Three-Dimensional
769   Reconstruction of Cardiac Sarcoplasmic Reticulum Reveals a Continuous Network Linking
770   Transverse-Tubules. *Circulation Research* **113**, 1219-1230,
771   doi:doi:10.1161/CIRCRESAHA.113.301348 (2013).
772 33   Midgett, M., Thornburg, K. L. & Rugonyi, S. Blood Flow Patterns Underlie Developmental Heart
773   Defects. *American Journal of Physiology - Heart and Circulatory Physiology* **312**, H632-H642,
774   doi:10.1152/ajpheart.00641.2016 (2017).

775   34   Genoud, C., Titze, B., Graff-Meyer, A. & Friedrich, R. W. Fast Homogeneous En Bloc Staining of
776   Large Tissue Samples for Volume Electron Microscopy. *Frontiers in Neuroanatomy* **12**,
777   doi:10.3389/fnana.2018.00076 (2018).
778   35   Karnovsky, M. J. A formaldehyde-glutaraldehyde fixative of high osmolality for use in electron-
779   microscopy. *Journal of Cell Biology* **27**, 137-138A (1965).
780   36   Wainrach, S. & Sotelo, J. R. Electron microscope study of the developing chick embryo heart.
781   *Zeitschrift für Zellforschung und Mikroskopische Anatomie* **55**, 622-634,
782   doi:10.1007/BF00384502 (1961).
783   37   Manasek, F. J. Histogenesis of the embryonic myocardium. *American Journal of Cardiology* **25**,
784   149-168, doi:10.1016/0002-9149(70)90576-X (1970).
785   38   Mukherjee, K. *et al.* Analysis of Brain Mitochondria Using Serial Block-Face Scanning Electron
786   Microscopy. *JoVE*, e54214, doi:doi:10.3791/54214 (2016).
787   39   Butcher, J. T., Sedmera, D., Guldberg, R. E. & Markwald, R. R. Quantitative volumetric analysis of
788   cardiac morphogenesis assessed through micro-computed tomography. *Developmental*
789   *Dynamics* **236**, 802-809 (2007).
790   40   Hopkins, T. M. *et al.* Combining Micro-Computed Tomography with Histology to Analyze
791   Biomedical Implants for Peripheral Nerve Repair. *Journal of neuroscience methods* **255**, 122-130,
792   doi:10.1016/j.jneumeth.2015.08.016 (2015).
793   41   Karreman, M. A. *et al.* in *Methods in Cell Biology* Vol. 140 (eds Thomas Müller-Reichert & Paul
794   Verkade) 277-301 (Academic Press, 2017).
795   42   Morales, A. G. *et al.* Micro-CT scouting for transmission electron microscopy of human tissue
796   specimens. *Journal of Microscopy* **263**, 113-117, doi:doi:10.1111/jmi.12385 (2016).
797   43   Sengle, G., Tufa, S. F., Sakai, L. Y., Zulliger, M. A. & Keene, D. R. A Correlative Method for Imaging
798   Identical Regions of Samples by Micro-CT, Light Microscopy, and Electron Microscopy: Imaging
799   Adipose Tissue in a Model System. *Journal of Histochemistry & Cytochemistry* **61**, 263-271,
800   doi:10.1369/0022155412473757 (2012).
801   44   Deerinck, T. J. *et al.* Enhancing Serial Block-Face Scanning Electron Microscopy to Enable High
802   Resolution 3-D Nanohistology of Cells and Tissues. *Microscopy and Microanalysis* **16**, 1138-1139,
803   doi:10.1017/S1431927610055170 (2010).
804   45   Tapia, J. C. *et al.* High-contrast en bloc staining of neuronal tissue for field emission scanning
805   electron microscopy. *Nature Protocols* **7**, 193, doi:10.1038/nprot.2011.439 (2012).
806   46   Mikula, S. & Denk, W. High-resolution whole-brain staining for electron microscopic circuit
807   reconstruction. *Nature Methods* **12**, 541, doi:10.1038/nmeth.3361 (2015).
808   47   Cazaux, J. From the physics of secondary electron emission to image contrasts in scanning
809   electron microscopy†. *Microscopy* **61**, 261-284, doi:10.1093/jmicro/dfs048 (2012).
810   48   Kiserud, T. Physiology of the fetal circulation. *Seminars in Fetal and Neonatal Medicine* **10**, 493-
811   503, doi:10.1016/j.siny.2005.08.007 (2005).
812   49   Dzialowski, E. M. Comparative physiology of the ductus arteriosus among vertebrates. *Seminars*
813   *in Perinatology* **42**, 203-211, doi:https://doi.org/10.1053/j.semperi.2018.05.002 (2018).
814   50   Iacobazzi, D. *et al.* Cellular and molecular basis of RV hypertrophy in congenital heart disease.
815   *Heart (British Cardiac Society)* **102**, 12-17, doi:10.1136/heartjnl-2015-308348 (2016).
816   51   Jenni, R., Rojas, J. & Oechslin, E. Isolated noncompaction of the myocardium. *New England*
817   *Journal of Medicine* **340**, 966-967 (1999).
818   52   Weiford, B. C., Subbarao, V. D. & Mulherm, K. M. Noncompaction of the ventricular myocardium.
819   *Circulation* **109**, 2965-2971 (2004).
820   53   Finsterer, J., Stollberger, C. & Towbin, J. A. Left ventricular noncompaction cardiomyopathy:
821   cardiac, neuromuscular, and genetic factors. *Nat Rev Cardiol* **14**, 224-237,
822   doi:10.1038/nrcardio.2016.207 (2017).

823   54   Sedmera, D., Pexieder, T., Rychterova, V., Hu, N. & Clark, E. B. Remodeling of chick embryoniv
824   ventricular myoarchitecture under experimentally changed loading conditions. *The Anatomical*
825   *Record.* **254**, 238-252 (1999).
826   55   Hamburger, V. & Hamilton, H. L. A series of normal stages in the development of the chick
827   embryo. *Developmental Dynamics* **195**, 231-272, doi:10.1002/aja.1001950404 (1992).
828   56   Tobita, K., Garrison, J. B., Liu, L. J., Tinney, J. P. & Keller, B. B. Three-dimensional myofiber
829   architecture of the embryonic left ventricle during normal development and altered mechanical
830   loads. *The Anatomical Record Part A: Discoveries in Molecular, Cellular, and Evolutionary Biology*
831   **283A**, 193-201, doi:10.1002/ar.a.20133 (2005).
832   57   Ronneberger, O., Fischer, P. & Brox, T. in *Medical Image Computing and Computer-Assisted*
833   *Intervention – MICCAI 2015.* (eds Nassir Navab, Joachim Hornegger, William M. Wells, &
834   Alejandro F. Frangi) 234-241 (Springer International Publishing).

835